PRODUCTION CROSS SECTIONS OF METASTABLE XENON ISOTOPES VIA INELASTIC SCATTERING

Submitted by

Angela White

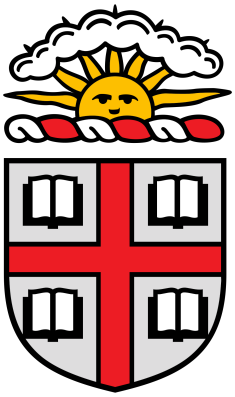

APRIL 2021

Department of Physics
Brown University

ABSTRACT

26 % of the energy density of the universe comes from dark matter. There are many theorized particle candidates for dark matter, and the Weakly Interacting Massive Particle is one of the strongest contenders. The Large Underground Xenon experiment, whose detector ran from 2013 to 2016, was a dark matter direct detection experiment which aimed to clearly detect or exclude WIMPs with spin-independent WIMP-nucleon cross section of 2×10^{-46} cm^2. Ultimately, LUX placed strong constraints on the WIMP-nucleon cross section but did not detect a WIMP-nucleon interaction. LUX was a two-phase xenon detector, and in order to calibrate the detector for its WIMP search, a stream of mono-energetic 2.45 keV neutrons was produced and launched into the detector's active xenon region. This analysis utilizes data from the period surrounding one 2015 neutron calibration of LUX to make a first measurement of the inelastic neutron scattering production cross sections of ^{131m}Xe and ^{129m}Xe. In addition, this analysis compares the the inelastic neutron scattering production cross sections calculated from LUX data to the effective inelastic neutron scattering production cross sections used by the particle physics simulation toolkit GEANT4, and finds that GEANT4's method of calculating inelastic final states does not successfully reproduce experimental values in the case of ^{131m}Xe and ^{129m}Xe.

ACKNOWLEDGMENTS

I am immensely grateful to my thesis advisor, Rick Gaitskell, for his patience, guidance, and advice over the course of the last year. Thanks also to Will Taylor, whose help was invaluable every step of the way, and who eased the strangeness of an entirely remote thesis. I would also like to thank Brown University's Physics Department at large for an excellent undergraduate education and everybody in Professor Gaitskell's lab for creating such a welcoming and fascinating learning environment.

I would also like to thank my roommate Grace, who due to the pandemic has been unable to escape me or this thesis, and whose patience and generosity has kept me sane. Likewise, my thanks to Livia and Justin for weathering the last four years with me like absolute champions.

TABLE OF CONTENTS

LIST OF FIGURES

LIST OF TABLES

LIST OF SYMBOLS AND ABBREVIATIONS

Term	Abbreviation
Deuterium-Deuterium	DD
Large Underground Xenon (Detector)	LUX
Sanford Underground Research Facility	SURF
Weakly Interacting Massive Particle	WIMP
Wimp Search	WS
Xenon	Xe

1. Dark Matter

1.1 Evidence for Dark Matter

In the 1930s, Fritz Zwicky estimated the mass of the Coma galaxy cluster and, using his estimate, made a prediction concerning the dispersion about the mean of galaxy velocities within the cluster. When his prediction proved to fall two orders of magnitude below the observed velocity dispersion of the cluster, Zwicky hypothesized the presence of “dark matter” in the cluster to explain the disparity. In order to account for the disagreement, Zwicky found that there would have to be considerably more dark matter than luminous matter in the cluster [22]. By "dark matter", Zwicky only intended to refer to matter that was not, for whatever reason, luminous, but as inconsistencies between cosmological predictions and measurements continued cropping up, the term would come to refer to non-baryonic matter. In 1978, building off of the analyses of Morton Roberts, Jaan Einasto, Albert Bosma, and numerous others, Vera Rubin and Kent Ford published a strong argument for unseen galactic matter in a paper on the observed rotational velocity of spiral galaxies. Rather than observing Keplerian rotation, as would befit a galactic disk with a centralized mass, Rubin and Ford observed rotational velocities which increased proportional to the radius before leveling out into a more or less constant value at large radii. These results were replicated in subsequent studies, and implied the existence of unseen coronas of non-trivial mass density surrounding visible galactic disks. Without these invisible but massive coronas, the galaxies would not have sufficient gravitational self-attraction to remain bound together [21].

Since Rubin’s study, more compelling evidence for the existence of unseen matter has

emerged. Gravitational lensing can provide measurements of dark matter halos surrounding galactic clusters. In the theory of general relativity, gravity is geometry. The presence of any mass warps flat space-time, giving it a non-zero curvature with geodesics that differ from those characteristic to flat space-time. Consequently, light passing by a large mass in space will temporarily cease to travel in a straight line, instead bending in accordance with the geodesic of the mass's local curvature. When light from an object behind a galaxy cluster is bent like this by the cluster's mass, the image of the luminous object can appear brighter than it ought, distorted, or sheared. The mass of the cluster determines the degree to which space-time warps, and it therefore also determines the distortion passing light rays will experience. Since the distortions are so closely linked to the mass of the lensing object, measurements of lensing shear can be used to estimate the total mass and approximate shape of the cluster's luminous and non-luminous components. Any massive object can cause lensing; in the case of an individual galaxy, the unseen mass causing lensing distortions can extend hundreds of kiloparsecs beyond the galactic center, well beyond the extent of luminous mass and further than rotational velocity curve studies can probe.

Another dark matter measurement concerns the very existence of intergalactic gas in galaxy clusters. When the mass of luminous matter in the cluster is estimated and compared to the mass and distribution of intergalactic gas throughout the cluster, astronomers find that the luminous mass is insufficient to account for the presence of the gas. Without dark matter deepening the potential wells of clusters, the large masses of hot, intergalactic gas bound in clusters would simply evaporate. Since the gas is very visibly in existence and gravitationally bound, it presents a convincing argument for the existence of dark matter in galaxy clusters.

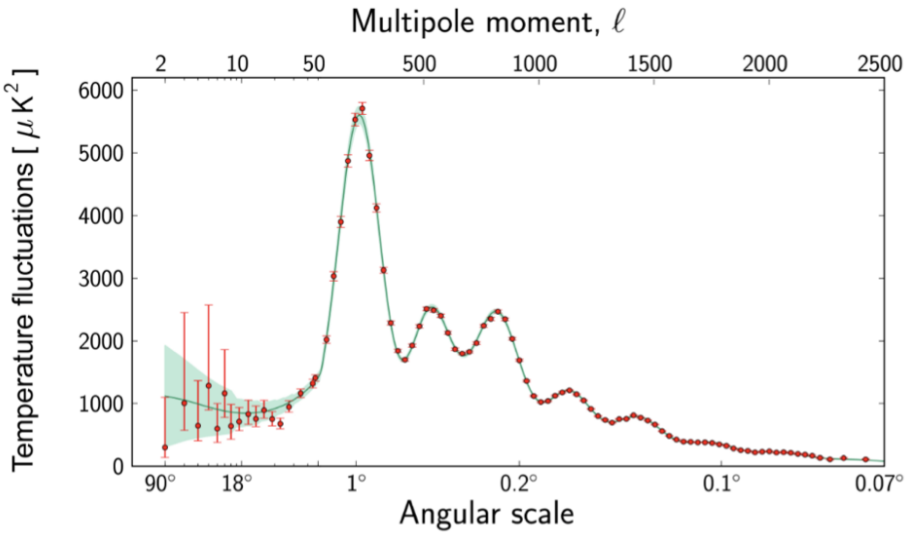

Figure 1-1: Planck's power spectrum of temperature fluctuations in the CMB. Fluctuations manifest at different angular scales on the sky, and can be used to calculate cosmological parameters. Plank data is represented by the red dots with error bars. The green curve represents the standard model of cosmology, ΛCDM. Image Source: [14]

The Cosmic Microwave Background (CMB) also provides evidence for the existence of dark matter. At a redshift of 1100, the universe had cooled enough that photons decoupled from baryonic matter. Photons from this decoupling have been redshifted into microwave wavelengths and are still streaming through the universe, forming the Cosmic Microwave Background. The CMB is nearly homogeneous, but small variations on the order of a fraction of a degree exist. The acoustic peaks of the CMB's temperature power spectrum (see Figure 1-1) places constraints on cosmological parameters [1]. The angular location and scale of each peak carries information about the energy density, and therefore the structure, of the universe. The first peak's angular location indicates that the universe is geometrically flat. The second peak's scale reveals that only 5% of the universe's energy comes from baryonic matter. Information from the remainder of the peaks, combined, tells

cosmologists that 26% of the universe's energy density is stored in dark matter [15].

1.2 Dark Matter Candidates

Many dark matter candidates have been proposed since the idea of dark matter itself became widely accepted in the 1980s. Several candidates have also been ruled out. MACHOS fall into the latter camp–MAssive Compact Halo Objects. The term MACHO serves as an umbrella term and refers to primordial black holes, faint stars, white dwarfs, and other stellar remnants. Since MACHOs are highly massive stellar objects theorized to populate galactic halos, a gravitational lensing technique called microlensing can be used to search for MACHOs in the Milky Way. Several microlensing experiments have done exactly that, and while a non-negligible percentage of galactic halo mass may be comprised of MACHOS (possibly up to 15%), experimental results indicate that massive, compact halo objects in the Milky Way cannot account for all of the mass in a galactic dark matter halo [14].

Axions, also called WISPs (Weakly Interacting Slim Particles), are another dark matter candidate. Axions arise naturally as a solution to Quantum Chromodynamics' strong-CP problem. In the QCD Lagrangian, a term related to the phase of the QCD vacuum must be extremely small, on the order of 10^{-10}, in order to avoid charge-parity violations. In 1977, Peccei and Quinn proposed a global U(1) symmetry that solved the strong-CP problem but also implied the existence of a new Nambu-Goldstone boson which was given the name "axion". To fit within experimental constraints, axions must be very light and interact with other forms of matter only rarely [11]. These characteristics make them a good dark matter

candidate, provided their mass lies in the approximate range between 10^{-3} and 10^{-6} eV [14]. In 2020, the Xenon1T collaboration reported an excess of electronic recoils measured in their detector. This excess could be caused by axions produced in the sun streaming though the detector and scattering off xenon atoms; however, it could also be caused by unexpected tritium or ^{37}Ar decays, and this possibility must be ruled out before any conclusions can be drawn. Even if solar axions are proven to exist by future generations of the XENON experiment, it will not definitively prove that axions are the cosmological dark matter predicted by CMB fluctuations. However, a direct detection of axions would put axions in the lead as the most compelling dark matter candidate [10].

Another potential dark matter candidate is called the sterile neutrino. The three flavors of neutrino predicted by the Standard Model (electron, muon, and tau neutrinos) are much too light to qualify as dark matter candidates. Our current understanding of the early universe suggests that fine structures formed in the universe before larger structures did. In order to reproduce this timeline, dark matter needs to have "frozen-out" of thermal equilibrium relatively early. Such "cold" dark matter must have a fairly large mass, since lighter particles would remain relativistic for longer. The Standard Model's three neutrino flavors are light enough that they would remain relativistic long enough to result in the inverted formation of large-scale structures before small-scale structures. However, a theoretical fourth flavor of neutrino with a very small mixing angle and no ability to interact with any force besides gravity could fulfill the necessary characteristics of a cold dark matter particle. A large mass relative to the other three neutrinos would ensure a small mixing angle, which coupled with the lack of weak interactions could explain why no neutrino detectors have reported detecting a fourth flavor. The sterile neutrino theory is considered attractive because, to date,

no left-handed neutrinos have been detected experimentally. Sterile neutrinos could explain this dearth of left-handed neutrinos. The experimental basis for the sterile neutrino stems from the unexpected excesses of electron neutrinos measured by the Liquid Scintillator Neutrino Detector and MiniBooNE at Fermilab. Thus far, however, there has been no conclusive evidence in support of a fourth, "sterile" neutrino flavor [11].

One of the strongest dark matter candidates at the moment is the WIMP (Weakly Interacting Massive Particle). WIMPs are cold dark matter particles which are theorized to only interact with baryonic matter through the weak and gravitational forces. Their predicted mass falls in the 1 GeV to 10 TeV mass range [14].

WIMP particles, much like axions, crop up naturally in theories entirely separate from dark matter hypotheses. Supersymmetric models predict WIMP-like particles, as do models of universal extra dimensions and the little Higgs scenario. The strongest argument in favor of WIMPs is something called the WIMP miracle. In the very early universe, particles existed in thermal equilibrium; particles and their antiparticles were created and annihilated at equal rates. As the universe expanded, it cooled, and once the temperature of the universe dropped below the mass of a WIMP particle, WIMP particles and antiparticles decoupled from equilibrium. Out of equilibrium, WIMP particles and antiparticles annihilated each other until the continued expansion of the universe rendered the rate of annihilation negligible. Assuming the annihilation cross-section of WIMPs is dependent upon the weak force, the predicted abundance of WIMP particles left in the universe once the annihilation stopped matches the known, measured mass density of dark matter from the CMB power spectrum [16]. This coincidence, called the WIMP Miracle, makes WIMPs an especially attractive dark matter candidate.

1.3 Indirect Detection

Although the rate of WIMP annihilation in the universe today is negligible compared to that of the early universe, WIMPs still undergo annihilation in any region of high WIMP density. Neutrinos, electron-positron pairs, and photons are all expected products of WIMP annihilation. Detectors like the Fermi Gamma Ray Space Telescope (Fermi-LAT) and IceCube can look for WIMP annihilation indirectly by searching for excesses of electrons, positrons, neutrinos, or photons of a certain energy emitting from regions of high theoretical WIMP density, like the Sun, the Galactic Center, dwarf galaxies, or galaxy clusters. Fermi-LAT has measured an excess of gamma-ray emission out of the Galactic Center, but WIMP annihilation is only one of many valid theories with the potential to explain gamma ray emission exceeding theoretical expectations in the Galactic Center [14].

1.4 Direct Detection

While indirect detection experiments looking for WIMPs have yet to produce any conclusive results, direct detection methods have set constraints of increasing strictness on the WIMP mass. In direct detection experiments, rather than looking for WIMP annihilation products in cosmological regions of high theoretical WIMP density, the density of the dark matter halo of the Milky Way is utilized and annihilations are largely ignored. Rather than waiting for a WIMP-WIMP interaction, direct detection experiments look for signals from WIMP-nucleon interactions (weak interactions with atomic nuclei). The detector counts these interactions by detecting the energy deposits from recoils off atomic nuclei. The dark

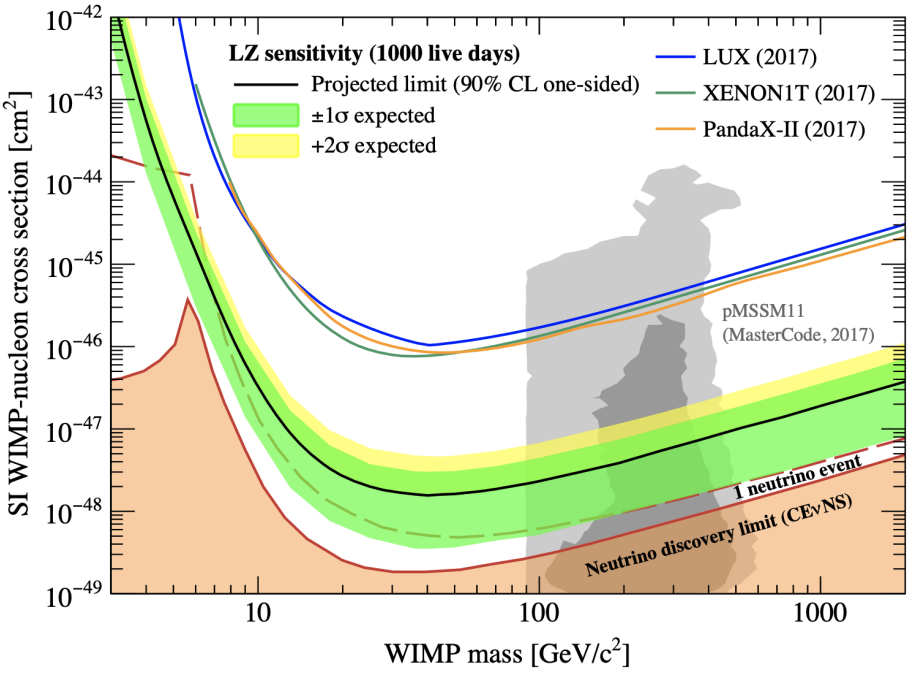

Figure 1-2: Constraints placed on spin-independent WIMP-nucleon elastic scattering from several completed direct detection experiments using liquid xenon, together with the predictions for constraints placed by the LZ detector, which is still under construction. The lower shaded region and dashed line indicate the limitations from the coherent scattering of neutrinos and the grey contoured regions show favoured regions from pMSSM11 model scans. Image Source: [18]

matter halo in the neighborhood of Earth has a density of approximately $\rho \approx 0.4$ GeV/cm^2, moving at approximately 235 km/s relative to Earth. The motion of the Earth about the sun should cause the rate of detected WIMPs to fluctuate over the course of a year. Thus far, no direct detection experiments have measured any WIMP , but every search provides a new limit on the WIMP-nucleon cross-section. Figure 1-2 plots several of these constraints, as well as several regions that the future LZ experiment will be able to probe in search of weakly interacting, massive particles [14][18].

2. The LUX Experiment

The LUX (Large Underground Xenon) detector was a direct detection WIMP experiment which completed its data-taking period in 2016 and reported its final constraints on the WIMP mass and scattering cross section in 2017. LUX was located in the Davis cavern at the Sanford Underground Research Facility (SURF) in South Dakota, 4850 feet below ground. The LUX detector aimed to clearly detect or exclude WIMPs with spin-independent WIMP-nucleon cross section of 2×10^{-46} cm^2. Such a cross section is equivalent to a scattering rate of approximately 1 event/100 kg/month in the central 100-kg fiducial volume of the detector [6].

2.1 LUX Detector Design

The LUX experiment consists of a two-phase xenon detector suspended within a tank of purified water. Xenon, as an inert gas with no naturally occurring radioactive isotopes, provides a low-background target for the WIMP search. The detector utilizes purified liquid xenon, as well as a gaseous xenon region, to measure scintillation photons and ionization electron signals from nuclear and electronic recoils occurring in the liquid xenon region [6]. A 20 tonne steel shield and a 300 tonne water shield surround the detector itself [9]. Within this water shield, the detector consists mainly of two nested, titanium cryostats with a vacuum maintained between them in order to sustain 370 kg of xenon in the liquid phase [8]. Prior to LUX, no large, dark matter direct detection experiments used titanium. Titanium was selected in the case of LUX for its tensile strength (superior to copper's) and

its ability to be welded. Copper cannot be welded and must be brazed, which can leave holes. Using titanium rather than copper avoids these micro-holes and the potentially radioactive contaminants they can allow in, like radon [8]. Since radon decays contribute significantly to the background of underground detectors, any steps to reduce radon contamination are key to keeping the background signals in the detector low.

Although the LUX detector holds 370 kg of liquid xenon, only 250 kg are considered "active" in the time-projection chamber (TPC). The TPC is the region of the detector in which particle interactions can be detected, tracked, and recorded. Three wire grids form the electric field that permeates the liquid xenon in the LUX detector: the cathode at the base of the detector, the gate, which is slightly below the liquid level, and the anode, which is above the gaseous xenon region. The TPC is 48 cm high, measuring from the cathode to the gate, with a diameter of 47 cm. Above the 250 kg of liquid xenon in the TPC, a gaseous xenon region extends for 1 cm [3]. An array of 61 photomultiplier tubes (PMTs) above the gaseous xenon measure light signals from electroluminescence, and an additional array of 61 PMTs measuring gamma rays from prompt scintillation is located below the active region of liquid xenon. Each PMT is sensitive to singular photons [4]. Additional grids shield the PMTs from interference by electric fields created by the anode and cathode [3]. During grid conditioning for the 2014-2016 data run, charge built up on the detector's polytetrafluoroethylene (PTFE) walls, resulting in a variable electric field across the fiducial region of the xenon which measured 30 V/cm at the bottom of the TPC and 600 V/cm at the top [16]. The ramifications of this variable electric field will be discussed in greater detail in section 3.3.

Four thermosyphons located at the top, bottom, and sides of the detector maintain

a lowered temperature of 160 K via the evaporation of liquid nitrogen. A continuous circulation system in the detector passes the xenon through a heated zirconium getter in order to filter out impurities like oxygen, water vapor, and ^{83m}Kr [16]. A CAD reconstruction of the geometry of the inner detector is given by Figure 2-1.

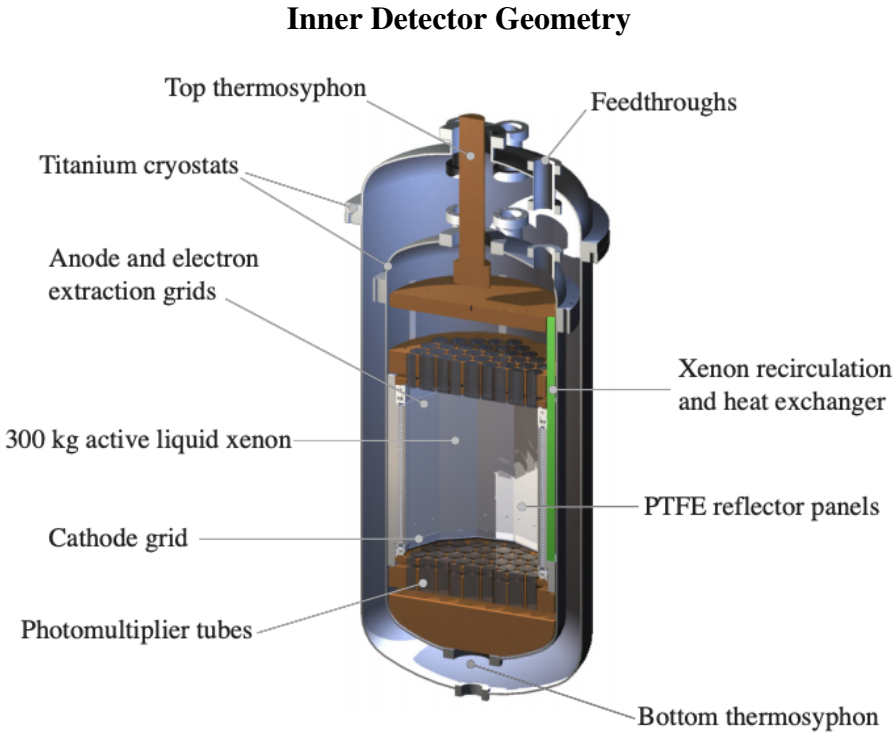

Figure 2-1: Geometry of LUX detector within the water tank: Xenon is cooled to 160 K, with 61 photomultiplier tubes (PMTs) above and below the Xenon. Image Source: [6]

2.2 Signal Production

When particles interact with the xenon in the active xenon region, they deposit their energy in the detector by scattering off of an atomic electron cloud or nucleus. If the particle scatters off of the electron cloud, the resulting electronic recoil (ER) can release

heat, scintillation photons and ionization electrons into the detector. In the case of electronic recoils, the amount of energy lost to heat is negligible. If the particle scatters off of the atomic nucleus, the nuclear recoil (NR) can likewise result in the release of heat, scintillation photons, and ionization electrons. Different type of particles scatter off of xenon atoms differently: gamma rays, x-rays, and beta particles cause electronic recoils, while both WIMP particles and neutrons produce nuclear recoils. For nuclear recoils, the amount of energy lost to heat increases with the amount of energy deposited, while the amount of energy lost to heat in an electronic recoil is negligible at all energies [16].

Nuclear and electronic recoils in the detector thus deposit energy into the detector through some combination of ionization electrons and scintillation photons. However, PMTs can only detect photons, not electrons. In the detector, an NR or ER interaction produces a number of scintillation photons which the PMTs detect nanoseconds after the event. This first signal is termed S1, and it is proportional to the number of photons that the PMTs detect. For the ionization electrons, the electric field maintained by the detector's cathode and anode draws any electrons produced by the interaction upwards, into the gaseous xenon. The electric field is also much stronger in the gaseous xenon, and the stronger field allows ionization electrons to strike xenon atoms and excite them, releasing photons through electroluminescence. The excited gaseous xenon atoms emit photons as they relax back to lower energy states. The photons from the de-excitation are detected by the PMTs and form a signal called S2. Although it is a more complicated calculation than S1, S2 is proportional to the number of ionization electrons produced by a given interaction [19]. The TPC can map the x and y coordinates of interactions by tracking the x, y coordinates of the region of PMTs which detects the greatest S2 signal. S2 is used

for coordinates rather than S1 because the ionization electrons produce photons while in the gaseous region, at most a centimeter away from the PMTs. Consequently, the S2 signal has less time to spread and is much more localized. Determining the z-coordinate of an event relies on both S1 and S2. Since the electric field throughout the detector is static and electrons drift at a fixed rate of 1.5 cm/s, the difference in time between the detection of an S1 pulse and its corresponding S2 pulse can be used to extrapolate the z-coordinate of a particle-xenon interaction, as depicted in Figure 2-2 [19].

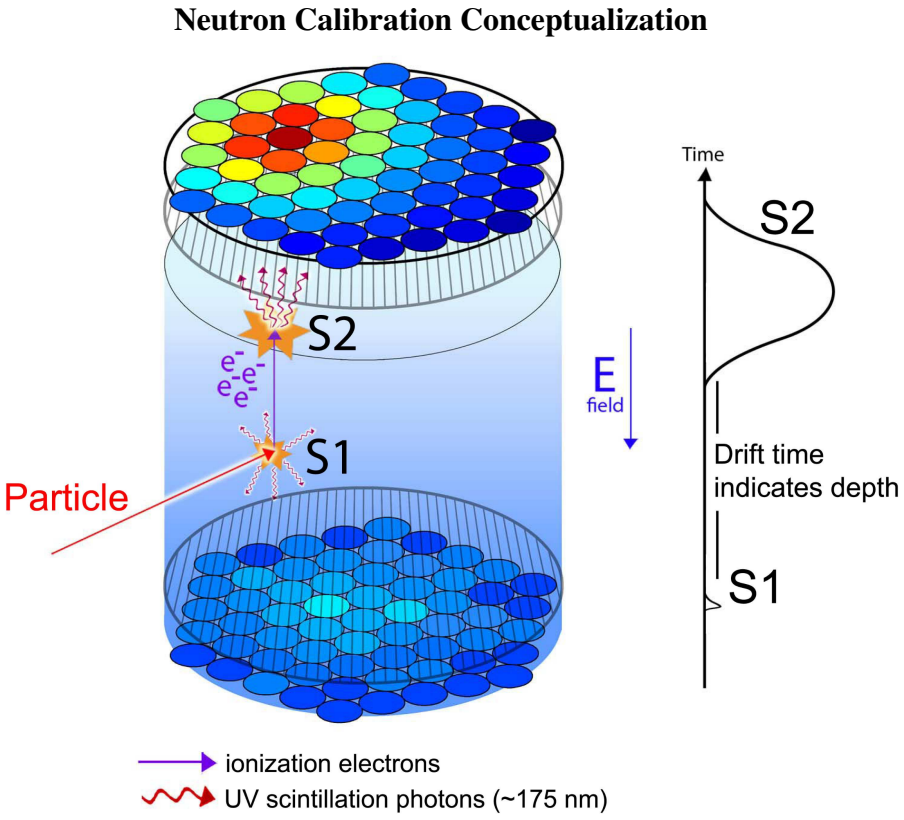

Figure 2-2: Conceptual diagram of a particle experiencing a single scatter in the active xenon volume. The neutron conduit begins at the water tank wall and ends just before the outer cryostat, where the particle enters. S1 signals register immediately while S2 signals require time to reach the gaseous xenon. Image Source: [6]

The combined energy is the total energy deposited in the detector by the scintillation photons and ionization electrons of a given event. For an electronic recoil, the combined

energy can be calculated with Equation 2.1, and for a nuclear recoil the combined energy is given by Equation 2.2. The energy-dependent function $f(E_{\mathrm{ee}})$ is a quenching factor, which describes the fraction of deposited energy lost to heat. For the electronic recoils, $f(E_{\mathrm{ee}}) = 1$, since the quantity of deposited energy lost to heat is effectively null.

$$E_{\mathrm{ee}} = W\left(\frac{S_1}{g_1} + \frac{S_2}{g_2}\right) \tag{2.1}$$

$$E_{\mathrm{nr}} = \frac{W}{f(E_{\mathrm{ee}})}\left(\frac{S_1}{g_1} + \frac{S_2}{g_2}\right) \tag{2.2}$$

The factors g_1 and g_2 describe the LUX detector's efficiency at detecting single S1 and S2 events. Since S1 is the number of scintillation photons the PMTs detect, dividing it by the efficiency at which the PMTs detect photons (the detector gain) reproduces the number of total scintillation photons the event should have emitted. S2 isn't quite the number of ionization electrons detected by LUX, since LUX doesn't detection electrons. Likewise, g_2 is not simply a photon-detecting efficiency, since the ionization electrons undergo multiple processes to produce the photons the PMTs detect. Nevertheless, dividing S2 by g_2 reproduces the total number of photons that should have been emitted by an event's ionization electrons. Multiplying this by the work function $W = 13.67$ eV outputs the total energy deposited through scintillation photons and ionization electrons by a given event [19].

2.3 Signal Background

LUX aimed to detect ~1 WIMP-nucleon interaction event/100 kg/month. The fiducial region from which events were selected to make this measurement was approximately 100 kg, so the background of the detector, at least for single-scatter events, needed to have <1 background event over the entire 300 day data-collection run which could potentially be interpreted as a WIMP signal in the fiducial volume [6]. In order to be misinterpreted as a WIMP interaction, an event must be a single scatter nuclear recoils in the active xenon region occurring within the energy within the energy range 3.4-25 keV_{nr}. The WIMP search energy range differs for nuclear recoil (NR) events and electronic recoils (ER) events, as each type of event has its own scintillation and ionization yield. The WIMP search background energy range for ER events is therefore 0.9-5.3 keV_{ee} [5].

Low energy ER events provide the dominant background in the 250 kg active xenon region, predicted to be $1.8 \pm 0.2_{stat} \pm 0.3_{sys}$ $mDRU_{ee}$ [4]. These electronic recoils are caused by radio-impurities in the construction materials of the detector itself. Tests on the titanium plates, sheets, and welding wires used to build LUX were run at the Low Background Facility at Berkeley Lab, the Oroville Counting Facility in northern California, and the SOLO facility in northern Minnesota [8]. Titanium samples stored at high altitudes were measured to have higher concentrations of ^{46}Sc decay due to cosmogenic activation, but the titanium was otherwise found to be a low-background material candidate for the detector. The data used in this thesis dates from 2015, and the LUX detector was moved below-ground in 2013. ^{46}Sc has a half-life of ~84 days, so it did not constitute a notable

source of background during LUX's 2015 data-taking [8]. Tables 2-3 and 2-4 list detector components with the most significant masses, as well as the details of the screening process which measured their contribution to the LUX detector's background.

Since the liquid xenon target has a relatively high density at 2.9 g/cm^3, gamma rays from detector components have a mean free path limited to several centimeters in the detector itself [5]. Thus, background signals from these shallowly-penetrating gamma rays can be minimized by excluding events which occur in the outer centimeters of the liquid xenon region during data analysis.

Component	Composition	Total Amount Used in LUX	Counting Facility	Counting Live Days	Quantity Counted
PMTs		122 PMTs	SOLO	See caption	4 ×5 PMTs
PMT bases		122 bases	SOLO	18	60 bases
Field ring supports (inner panels)	HDPE	18.0 kg	SOLO	14	1.4 kg
Field ring supports (outer panels)	HDPE	15.5 kg	SOLO	8.9	1.6 kg
Reflector panels (main)	PTFE	15.5 kg	SOLO	9.5	2.4 kg
Reflector panels (grid supports)	PTFE	9.3 kg	SOLO	6.7	2.0 kg
Cryostats	Ti	231 kg	Oroville	13	8.0 kg
Electric field grids	Stainless steel	4.5 kg	SOLO	7.3	37 kg
Field shaping rings	Cu	28 kg	SOLO	9.0	15 kg
PMT mounts	Cu	169 kg	SOLO	5.0	1.1 kg
Weir	Cu	3.2 kg	SOLO	7.5	4.8 kg
Filler chiller shield	Cu	293 kg	SOLO	–	–
Top shield	Cu	121 kg	SOLO	–	–
Superinsulation	Aluminized Mylar + polyester	2.2 kg	SOLO	13	0.6 kg
Thermal insulation	HDPE	6.0 kg	SOLO	11	4.5 kg

Figure 2-3: LUX detector components, their composition, the specifics of their screening, and the quantity of each material ultimately present in the LUX detector. Components without listed counting quantities were not counted, but are included due to the significance of their mass and their proximity to the detector's active xenon region. Image Source: [5]

Component	Counting Unit	Counting Results [mBq/unit]					
		^{238}U	^{226}Ra	^{232}Th	^{40}K	^{60}Co	Other
PMTs	PMT	<22	9.5±0.6	2.7±0.3	66±6	2.6±0.2	
PMT bases	base	1.0±0.4	1.4±0.2	0.13±0.01	1.2±0.4	<0.03	
Field ring supports (inner panels)	kg		<0.5	<0.35			
Field ring supports (outer panels)	kg		<6.3	<3.1			
Reflector panels (main)	kg		<3	<1			
Reflector panels (grid supports)	kg		<5	<1.3			
Cryostats	kg	4.9±1.2	<0.37	<0.8	<1.6	4.4±0.3 (^{46}Sc)	
Electric field grids	kg		1.4 ± 0.1	0.23 ± 0.07	<0.4	1.4 ± 0.1	
Field shaping rings	kg		<0.5	<0.8		<0.3	
PMT mounts	kg		<2.2	<2.9		<1.7	
Weir	kg		<0.4	<0.2		<0.17	
Superinsulation	kg	<270	73±4	14±3	640±60		
Thermal insulation	kg		130±20	55±10	<100		

Figure 2-4: LUX detector components and their corresponding radioassay data. More than 75 different materials underwent testing prior to the construction of the LUX detector; the above are the high-mass contributors to the detector. Reported radiation levels are for gamma ray lines in the titular isotope's sub-chain. All errors are statistical only, with upper limits at 90% confidence level. Image Source: [5]

The photomultiplier tubes' proximity to the active xenon region can lead to PMT radioactivity dominating the detector background. To prevent this, the LUX utilized Hamamatsu R8778 PMTs, chosen to maximize radiopure material composition and consequently minimize radiation [7]. As in the case of gamma rays from detector materials, background signals from the PMTs can be reduced by choosing a fiducial region several centimeters away from the PMT arrays at the edge of the xenon volume. The number of gamma rays passing through a 118 kg inner fiducial volume is four orders of magnitude less than the number of gamma rays penetrating the liquid xenon shallowly, so a cut of only a few centimeters can have a significant impact on background levels [5].

The xenon itself provides an additional potential source of background. In early 2013, the xenon was moved underground at Sanford after being processed for krypton removal and left at altitude above-ground for either 7 or 49 days, depending on the batch of xenon in question. The above-ground exposure time resulted in the production of cosmogenic xenon radioisotopes, including ^{127}Xe, $^{129\mathrm{m}}$Xe, $^{131\mathrm{m}}$Xe, and ^{133}Xe. These isotopes have half-lives of 36 days, 8.9 days, 12 days, and 5.3 days respectively. Since the data used in this analysis comes from 2015, two years and more than twenty ^{127}Xe half-lives after the xenon was moved below ground, backgrounds due to the decay of cosmogenic ^{127}Xe, $^{129\mathrm{m}}$Xe, ^{131m}Xe, or ^{133}Xe will not meaningfully contribute to the background in the reconstructed detector energy spectrum [8].

One source of background that time cannot mitigate is radon. Most soils naturally contain uranium, and the radioactive decay of this uranium results in the release of gaseous radon. Radon can also be released by the same decay in rocks and groundwater. In a below-ground laboratory like the Davis cavern, where LUX was located for the duration

of its underground runs, natural radon concentrations are higher than they would be above ground [2]. Thus, radon and its decay chain provide a considerable background for the LUX detector. ^{222}Rn is the most common radon radioisotope, and it's produced by ^{238}U's decay chain. ^{222}Rn has a 3.8 day half-life. ^{220}Rn, a product in ^{232}Th's decay chain, is also common and has a 56 second half-life. Due to its longer half-life, ^{222}Rn can be evenly mixed by the detector's filtration system throughout the detector's active region before it decays. Because ^{222}Rn is an isotope of an inert gas, the LUX circulation and filtration system does not eliminate it. Consequently, ^{222}Rn can exists in equilibrium throughout the detector, decaying in the active region and providing a non-negligible background [12].

Isotope	**Half-life $t_{1/2}$**	**Average Lifetime τ**	**Q-value (keV)**	**Decay Mode**
^{222}Rn	3.82 days	5.5 days	5590.3	α
^{218}Po	3.1 min	4.5 min	6114.7	α
^{214}Pb	26.8 min	38.7 min	1019	β
^{214}Bi	19.8 min	28.5 min	3270	β
^{214}Po	162.3 μs	234.1 μs	7833.5	α

Figure 2-5: ^{222}Rn decay chain characteristics above ^{210}Po, which is long-lived with a half-life of 22.23 years. Image Source: [12]

Radon enters the detector through sources exposed to radium, most likely during the manufacturing process of detector components, or through contamination of the laboratory. It's also a contaminant in the liquid xenon itself. In the course of its decay chain, the daughter isotope of most concern to this analysis is ^{214}Pb. ^{214}Pb undergoes a beta decay with 11% probability in the 100s of keV, with an overall decay rate in the detector's active region of 7.4 mBq. Because ^{214}Pb has a relatively lengthy half-life and is filtered out of the xenon at a constant rate, these decays are distributed homogeneously throughout the detector volume [19]. A Monte-Carlo simulation of the ^{214}Pb decay spectrum scaled to fit

data from the 85-day LUX run in 2013 is displayed in 2-6.

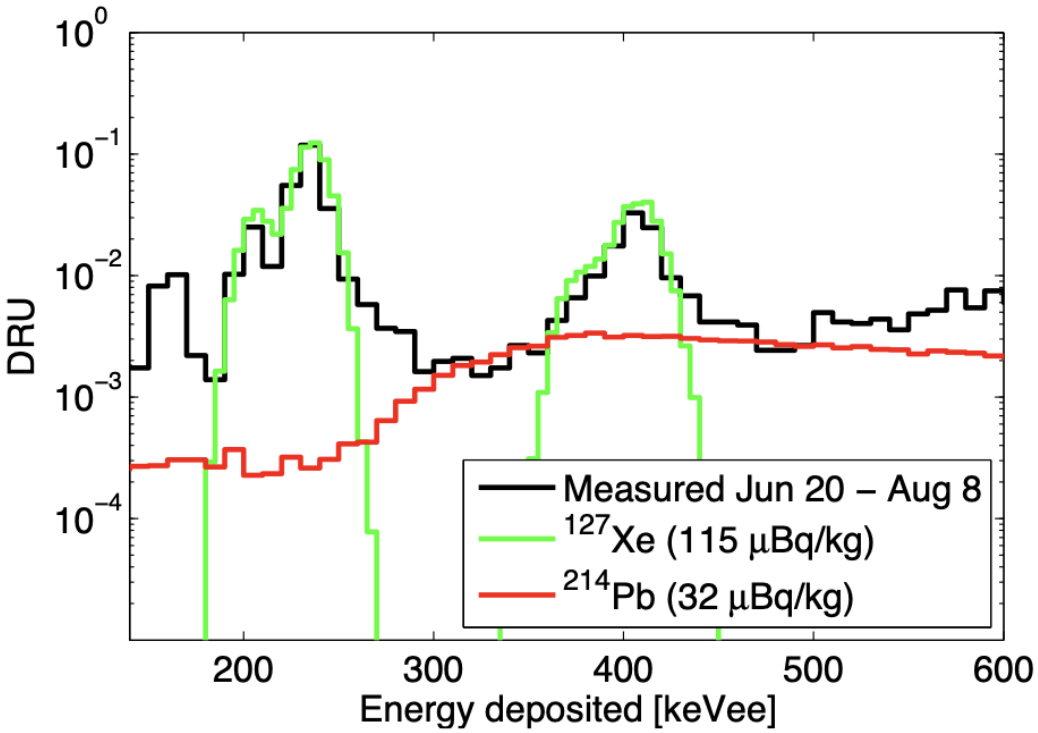

Figure 2-6: ^{214}Pb decay chain predictions scaled to compare to Run 3 LUX data. In Run 4, the decay features from cosmogenic ^{127}Xe will be heavily suppressed. Image Source: [19]

2.4 D-D Neutron Calibration

WIMPs are theorized to be massive, neutral particles that interact with xenon atoms via nuclear recoils. In order to calibrate the LUX detector for such particles and their interactions, the LUX experiment uses another species of large, neutral particles: neutrons. Neutron-xenon interaction cross sections are much larger than WIMP-xenon cross sections, and therefore provide numerous nuclear recoils by which to calibrate the detector. 2.45 MeV mono-energetic neutrons are produced by an Adelphi DD108 neutron generator outside the detector's water tank. In the neutron generator, D_2 gas is ionized using microwaves, and the

resulting D^+ ions are accelerated towards a V-shaped copper target by an applied electric field (see figure 2-7).

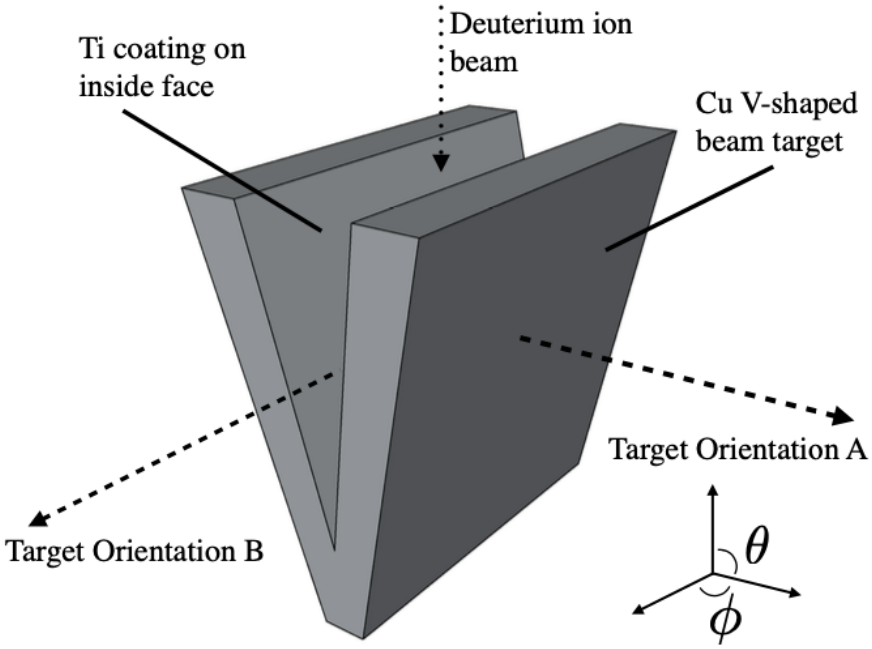

Figure 2-7: Titanium-coated, copper target in the D-D neutron generator. Image Source: [16]

The V-shaped target has a titanium coating, and D^+ ions embed themselves into the titanium before fusing with subsequent D^+ nuclei to complete the reaction in equation 2.3.

$$D + D = n + {}^3H \tag{2.3}$$

As shown in Figure 2-8, at an angle of $\frac{\pi}{2}$ relative to the D^+ ion beam, the neutrons emitted by the D-D fusion interactions have a uniform energy of 2.45 MeV.

Borated polyethylene shielding surrounds the detector except for a small portion which opens towards the water tank and an air-filled PVC tube, which the neutrons travel through

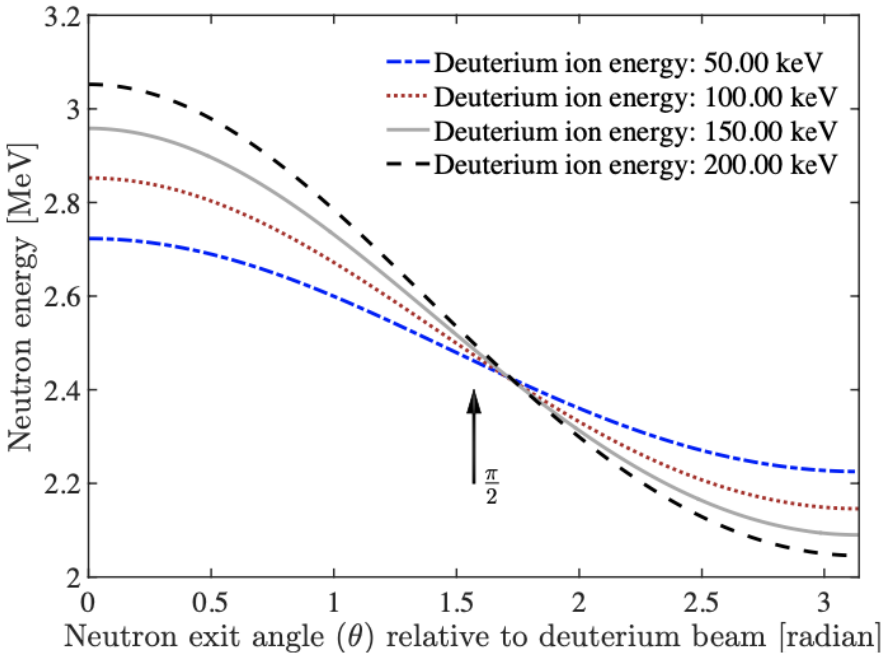

Figure 2-8: Neutron Energy from the D-D generator as a function of the exit angle relative to the incident D^+ ion beam. Image Source: [16]

in order to reach the detector cryostats. Neutrons which scatter out of the PVC pipe deposit their energy in the water tank rather than the detector. When the neutron calibration is not occurring, the PVC tube can be lowered to the bottom of the water tank in order to avoid additional radiogenic background. There is a 2 cm gap between the water tank walls and the collimator and the cryostats and the collimator [16].

2.5 BACCARAT Simulations and GEANT4

GEANT4 is a software package which aims to provide the tools to accurately simulate (in Monte-Carlo style simulations) the passage of particles through matter [13]. BACCARAT is a Geant4-based Monte Carlo simulation designed by the LUX Collaboration

specifically for the LUX detector's geometry, and it relies on GEANT4 to provide accurate system geometry, particle tracking, detector response, and constants for physics processes governing the particle interactions during the simulation. For this analysis, the cross-sectional values provided by GEANT4 are under scrutiny. Total cross sections and neutron capture cross-sections provided by GEANT4 are individual, energy-dependent values. For inelastic final states, there is no single, energy-dependent cross-section value in G4NDL, the GEANT4 cross-section database. Instead, final scattering states are defined by the energy of the incident neutron, the energy of the scattered neutron, and the angle of the scatter [13]. Convoluted documentation renders a more full understanding of the inelastic neutron scattering cross section difficult to acquire. Consequently, the inelastic neutron cross sections extracted from GEANT4 in this analysis will be calculated by treating simulated spectra as experimental data.

3. Finding Inelastic Production Cross Sections of Metastable ^{129}Xe and ^{131}Xe

The data used in this analysis is drawn from the 2014 to 2016, 360-day LUX data-collection run. A neutron calibration occurred from early October 1st to late October 13th 2015, activating the xenon in the detector. This period will be referred to as the October DD calibration period, so named for the Deuterium-Deuterium neutron calibration source (described in section 2.4). Data following this calibration period, spanning October 15th to October 28th, will be referred to as October WS data. WS stands for WIMP Search, as any period not involving a calibration falls under that umbrella. This analysis will focus on the xenon activation resulting from the calibration; in order to measure energy depositions stemming from the xenon activation, signals making up the detector's baseline background must first be excluded. Data spanning September 1st to September 31st, immediately preceding the calibration period, is used as the model for the LUX detector's background. Additional data from January 2015, February 2015, March 2015, June 2015, July 2015, and August 2015 were utilized to establish systematic error bounds on the LUX detector's combined energy spectra. The listed months were chosen for their lack of neutron calibration activation signals. Any datasets including ^{83}Kr or ^{137}Cs calibrations were excluded from this analysis. The variation in the background over time is evident in

All datasets utilized in this analysis were processed through the High Energy Golden Event Filter, hereafter referred to as HEF. All LUX data undergoes data processing in which pulses are classified as S1, S2, SE, SPE, or Else. S1 and S2 were defined in the previous

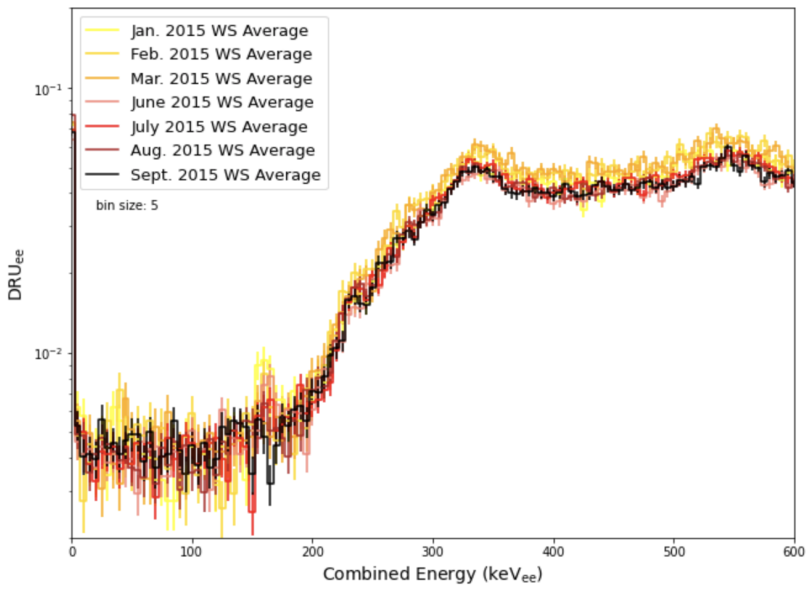

Figure 3-1: A time-varying background in the detector stems from the radon decay chain. The shape of the decay spectrum matches the decay spectrum for ^{214}Pb in Figure 2-6.

chapter. SE and SPE tag the detection of a single electron and a single photoelectron, respectively, and Else is a catch-all category for signals not fitting the other four profiles. The HEF extends this processing one step by counting the S1 and S2 signals in each event and selecting for events with only certain numbers and permutations of S1 and S2 pulses. This allows for the building of datasets comprised entirely of single, double, triple, or however many scatter events. Since WIMPS interact very weakly, they are expected to only scatter a single time in the active xenon region, so the HEF filter would be a helpful tool for filtering out unnecessary events. The filter also removes "spurious" pulses—because an S2 signal should lag behind its corresponding S1 signal, all S2 signals preceding the first S1 signal for a given event are discarded by the filter. Lower limits placed on S1 pulses and S2 pulses eliminate the gamma background from ^{238}U, ^{232}Th, ^{60}Co, and ^{40}K decay. The HEF

filter was specifically designed to efficiently select relevant events at high energies. For the purposes of this analysis, all datasets contain single scatter events only.

3.1 Research Questions and Motivation

The sensitivity of a liquid xenon detector like LUX depends upon the accuracy with which background rates in the detector are understood and can be separated out. Although LUX is no longer running, the LUX-ZEPLIN, PandaX-4t, XENONnT, DARWIN, and nEXO detectors all use liquid xenon and are in various stages of planning or construction. All of these detectors could benefit from a better understanding of neutron cross sections in xenon, and correspondingly more accurate simulated predictions. Currently, there is no accessible literature on the inelastic neutron production cross sections of ^{129m}Xe or ^{131m}Xe. GEANT4, the toolkit from which many particle physics simulations draw values like interaction cross sections, has no recorded value for the inelastic neutron scattering production cross sections of ^{129m}Xe or ^{131m}Xe. GEANT4's methods are described in greater detail in section 2.5. This analysis aims to use data from the 2014-2016 LUX data collecting period to calculate the inelastic neutron scattering production cross sections of ^{129m}Xe and ^{131m}Xe. The secondary goal of this analysis is to then compare the calculated cross sections to the simulated cross sections utilized by GEANT4 in order to determine the current reliability of GEANT4's method of simulating metastable xenon production.

3.2 Theoretical Foundations

The neutrons launched by the D-D generator into the liquid xenon during the LUX detector's calibration period can scatter elastically, inelastically, or merge with an atomic nucleus via radiative capture. The two interactions which result in significant energy depositions in the detector through electronic recoils are radiative capture (also called neutron capture) and inelastic scattering. The total production rate of a given isotope is equal to the number density (N) of its parent nuclei, multiplied by the sum of the thermal neutron flux multiplied by the neutron capture cross section and the fast neutron flux multiplied by the neutron inelastic scatter cross section [20].

$$R_{\text{total}} = N\left(\phi_{\text{t}}\sigma_{\text{capt.}} + \phi_{\text{f}}\sigma_{\text{inelast.}}\right) \tag{3.1}$$

Equation 3.1 can be split in two separate equations to solve for an isotope's production rate by neutron capture and its production rate by inelastic scatter. Metastable isotope states may be produced by inelastic scatters as well as neutron capture [17].

$$R_{\text{capt.}} = N\left(\phi_{\text{thermal}}\sigma_{\text{capt.}}\right) \tag{3.2}$$

$$R_{\text{inelast.}} = N\left(\phi_{\text{fast}}\sigma_{\text{inelast.}}\right) \tag{3.3}$$

The aim of this analysis is to calculate the production cross sections as given in equation 3.3 for $^{129\text{m}}$Xe and $^{131\text{m}}$Xe via inelastic scattering. The number densities (N) for

^{129}Xe and ^{131}Xe are known. Likewise, the fast neutron flux can be calculated using the cross-sectional area of the TPC and the neutron intensity during calibrations as given by the operation notes of the D-D neutron source. Thus, solving for the cross-sectional value first requires solving for the rate of production for each meta-stable state via neutron inelastic scattering. Combining equations 3.1, 3.2, and 3.3 demonstrates that the rate of production of an isotope by neutron capture, once subtracted from the total rate of a given isotope's production, returns the rate of production for an isotope through inelastic scattering.

$$R_{\text{inelast.}} = R_{\text{total}} - R_{\text{capt.}} \tag{3.4}$$

In equation 3.2, the number density N of the parent nuclei in the LUX detector is once again a known value, and the neutron capture production cross sections for all the isotopes involved in this analysis are likewise known, sourced from the JEFF-3.2 Evaluated Nuclear Data Library. However, the thermal flux of neutrons entering into the fiducial region of the LUX detector is unknown. Therefore, in order to calculate the inelastic neutron scattering production cross section of ^{129m}Xe and ^{131m}Xe, analysis must proceed in this order:

1. Find a unique decay signature in the range of 70 to 300 keV_{ee} from an isotope which is only produced via neutron capture. Use the signature from this isotope to measure thermal flux.

2. With the thermal neutron flux, calculate the neutron capture production rate of ^{129m}Xe and ^{131m}Xe.

3. Count the total number of decays for each metastable isotope during the October

WS period and subtract the number of those decays expected to come from nuclei produced by neutron capture. The remainder of decays belong to nuclei produced through inelastic neutron scattering.

4. Calculate the inelastic neutron scattering production rate of ^{129m}Xe and ^{131m}Xe, and from there calculate the inelastic neutron scattering production cross section for each metastable isotope.

Three separate equations derived from the nuclear decay equation enable the derivation of production rates during the DD calibration period using the combined energy deposition spectrum from the October WS period.

$$N_{\circ} = N_{\text{Decay}}\left(1 - 2^{\frac{-t_{WS}}{t_{\frac{1}{2}}}}\right)^{-1} \tag{3.5}$$

$$R_{\text{capt.}} = \frac{N_{\circ}}{V}\frac{ln(2)}{t_{\frac{1}{2}}}\left(1 - 2^{\frac{-t_{DD}}{t_{\frac{1}{2}}}}\right)^{-1} \tag{3.6}$$

$$\phi_{\text{thermal}} = \frac{R_{\text{capt}}}{N\sigma_{\text{capt}}} \tag{3.7}$$

Equation 3.5 uses the number of decay events counted for a given isotope in the combined energy spectrum of the October WS data to calculate the total number of atoms present at the beginning of the WS period, and therefore the end of the October DD calibration period. This value can then be plugged into equation 3.6 to find the neutron capture production rate for the isotope.

3.3 Event Selection

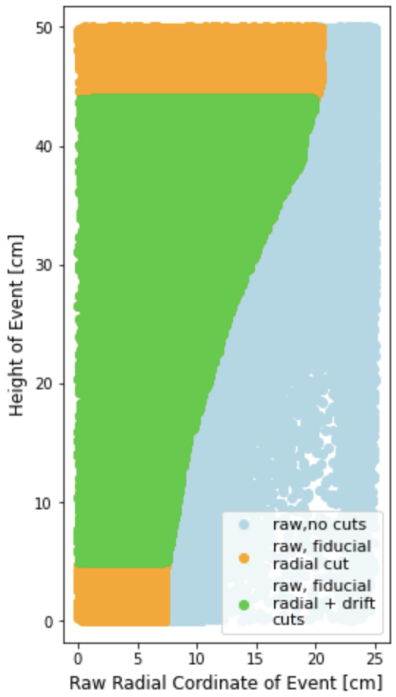

Figure 3-2: For an active xenon region with a radius of 25 cm and a height of 50 cm, a depth-dependent radial cut enforces a fiducial region of 105.4 kg while accounting for the inward drift of ionization electrons due to LUX's irregular electric field.

This analysis utilizes all single scatter events occurring in a 105.4 kg fiducial region of the LUX detector. The single scatter events are pre-selected by the HEF, and the fiducial cuts are made to enforce the fiducial mass within the liquid xenon detector.

1. Z-Coordinate Limits of Fiducial Region:

   - 40 μs < Drift Time < 300 μs: Since ionization electrons drift in the applied electric field at a constant rate of 0.15 $\frac{\text{cm}}{\mu\text{s}}$, this cut selects for events occurring more than 6 centimeters above the cathode and 3 centimeters below the gate.

2. Radial Coordinate Limit of Fiducial Region:

    - Due to the varying electric field across the detector during the 2014-2016 LUX data run, ionization electrons from events occurring at large radii low in the detector can be drawn towards the center of the detector as they move towards the gaseous xenon region. This drift could cause the top array of PMTs to incorrectly record the S2 pulse of an event outside the fiducial mass as originating inside of the fiducial radius. Consequently, the radial cut must vary with depth so that events occurring further from the surface of the liquid xenon are selected from within a smaller radius, therefore accounting for their larger radial drift. This cut can be seen in Figure 3-2.

3.4 Analysis

The first stage of analysis requires calculating the October WS period's ER combined energy deposition spectrum in the energy range of interest, 0-600 keV_{ee}, using Equation 3.4, restated below:

$$E_{ee} = W\left(\frac{S_1}{g_1} + \frac{S_2}{g_2}\right) \tag{3.8}$$

Error bars on the October WS data were derived from Poisson fluctuations of the dataset. The calculation of the combined energy for electronic recoils were repeated for the September WS data, which provided a baseline spectrum for energy depositions in LUX

105 kg Fiducial Volume: Oct. 2015 WS vs. Background Energy Spectrum Single Scatter HEF Data

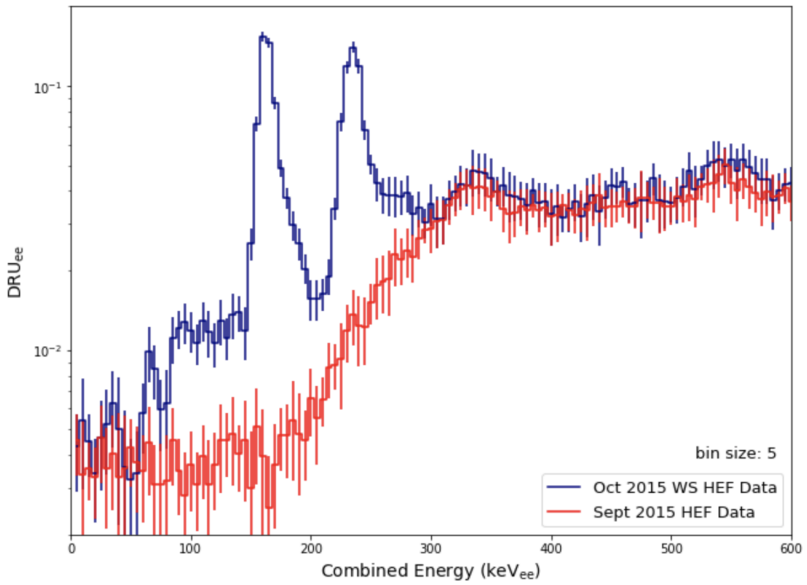

Figure 3-3: The single scatter decay rates calculated using combined energy with krypton calibration days excluded, plotted against the September WS with krypton calibration days likewise removed. The background has large systematic errors due to time-varying radon activity levels underground.

prior to the activation of the liquid xenon. However, because there is a time-varying radon background in the detector, additional systematic error was added to the statistical Poisson fluctuations of the September data. This systematic error was calculated by taking the difference of adjacent months' E_{ee} spectra for January, February, March, June, July, August, and September 2015, and adopting the range of differences as the upper and lower bounds of the variation for the radon background. Figure 3-3 shows the October WS spectrum plotted against the background spectrum. After 300 keV$_{ee}$, the error bars of the background spectrum overlap with the October WS spectrum, indicating that activation effects beyond that point are sub-dominant to the LUX detector's baseline radiation levels. The same holds true for energies below approximately 70 keV$_{ee}$.

The BACCARAT Monte Carlo simulations were used to produce decay spectra for

individual isotopes in the two weeks following the simulated neutron calibration of a simulated LUX detector. Plotting the individual decay spectra of all the isotopes expected as a result of xenon activation produces a simulated total spectra which, after the application of an energy dependent Gaussian convolution and feature-specific scaling, provides an isotope-by-isotope breakdown of the dominant decay sources in the real, background-subtracted data spectrum for the October WS period.

Simulated Decay Spectrum of Two Weeks Post Oct Calibration with Gaussian Convolution

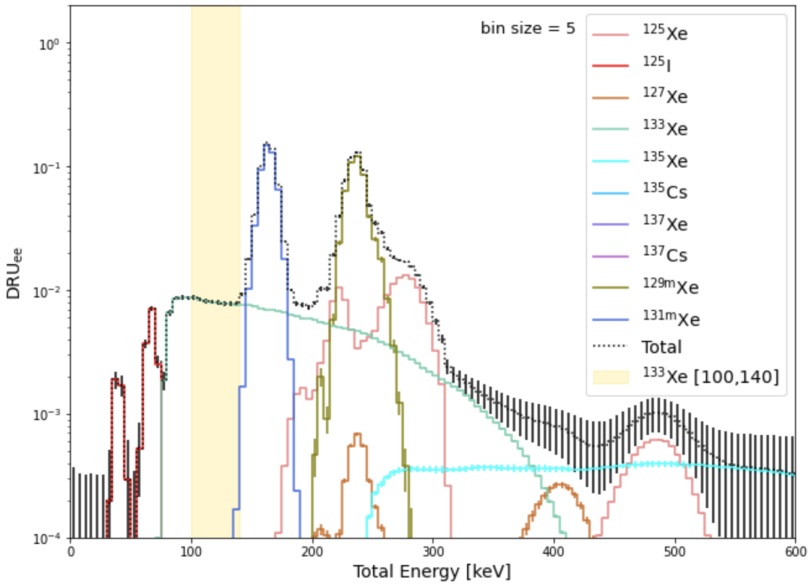

Figure 3-4: Simulation with 1e7 incident neutrons, with the Gaussian resolution determined by fitting individually to peaks. The highlighted region is dominated by the ^{133}Xe beta decay spectrum. ^{137}Cs, ^{135}Cs, and ^{137}Xe rates fall below the bounds of the y axis.

In order to calculate the thermal neutron flux, there must be a region in the decay spectrum which is dominated by a unique decay signature from an isotope produced solely through radiative transfer. Between 100 and 140 keV$_{ee}$, Xe133's beta decay dominates the simulated spectrum, as indicated by the yellow region in Figure 3-4.

Figure 3-5 plots the total simulated decay spectrum over the background-subtracted

105 kg Fiducial Volume: Background-Subtracted Oct. WS Single Scatter HEF Data vs Simulated Decay Spectrum

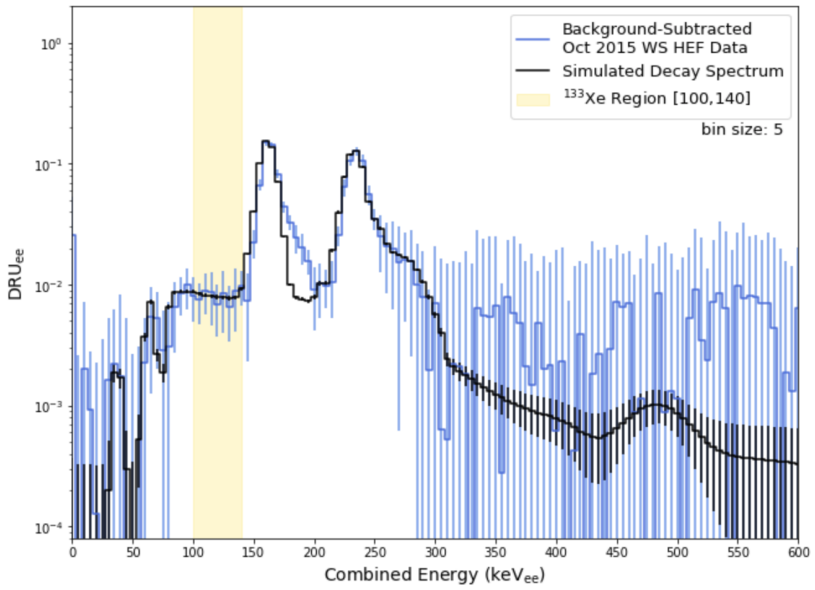

Figure 3-5: The October WS decay spectrum plotted against a simulated spectrum from BACCARAT. The yellow highlighted portion corresponds to the same region in Figure 3-3, demonstrating a region dominated by ^{133}Xe decays.

October WS combined energy spectrum. The simulated spectra, scaled spectrum-by-spectrum, matches the WS decay spectrum closely with the exception of the shoulder around 180 keV$_{ee}$. The source of the shoulder is unknown, and must be investigated further in future studies. Regardless, the close match of the simulated and real decay spectra supports the assumption that between 100 and 140 keV$_{ee}$, the combined energy spectrum is dominated by ^{133}Xe decays, and contributions from other decaying isotopes can be treated as negligible. The simulated spectrum predicts that 22.8% of all ^{133}Xe decays occur within the relevant energy region, so the total number of ^{133}Xe decays during the October WS period can be plugged into equations 3.5, 3.6, and 3.7 to obtain the thermal neutron flux in the LUX detector during the D-D calibration in October of 2015.

As Table 3.2 indicates, the calculated thermal neutron flux is 5.78 ± 0.62 $\times 10^{-5}$

^{133}Xe atoms Present at the End of the Calibration Period

Energy Region (keV)	Fraction of Total Decay Spectrum	Counted Decays	^{133}Xe Produced by DD
[100,140]	0.23	356 ± 45	2076 ± 263

Table 3.1: Calculation of ^{133}Xe atoms present in the Xenon at the end of the calibration period and the beginning of the WS period (Oct. 14th), presuming 5.24 day half-life and a 10.6 day livetime

Thermal Neutron Flux During Calibration

Production Rate ($cm^{-3}s^{-1}$)	^{132}Xe Capture Cross Section (cm^2)	^{132}Xe Fractional Abundance	Thermal Flux ($cm^{-2}s^{-1}$)
$(1.10 \pm 0.14)\times10^{-7}$	0.52×10^{-24}	0.269	$(5.78 \pm 0.73)\times10^{-5}$

Table 3.2: Calculation of thermal neutron flux presuming a 13 day calibration period

$cm^{-2}s^{-1}$. With the thermal neutron flux through the detector established, equation 3.6 can be applied for ^{125}Xe, ^{129m}Xe, and ^{131m}Xe. ^{125}Xe is also only produced via neutron capture, so the dominant decay branch of ^{125}Xe serves as a sanity check for the cross section calculation.

Oct. 2015 WS Decays from Isotopes Produced by Neutron Capture

Isotope	Parent Capture Cross Section (cm^2) (10^{-24})	Parent Fractional Abundance	Production Rate ($cm^{-3}s^{-1}$) (10^{-8})	Expected Decays (10^2)
^{125}Xe	177	0.001	14.9 ± 1.9	4.60 ± 0.58
^{129m}Xe	0.747	0.019	1.16 ± 0.15	1.61 ± 0.20
^{131m}Xe	0.665	0.041	2.19 ± 0.28	2.79 ± 0.35

Table 3.3: Calculation of thermal neutron flux presuming a 13 day calibration period and a 10.6 decay period

Table 3.3 lists the number of nuclei formed by radiative capture expected to decay during the October WS period for^{125}Xe, ^{129m}Xe, and ^{131m}Xe.

In order to use these decay values to establish inelastic neutron scattering cross sections, the total number of decays for each isotope during the October WS period must be

Simulated Decay Spectrum of Two Weeks Post Oct Calibration with Gaussian Convolution

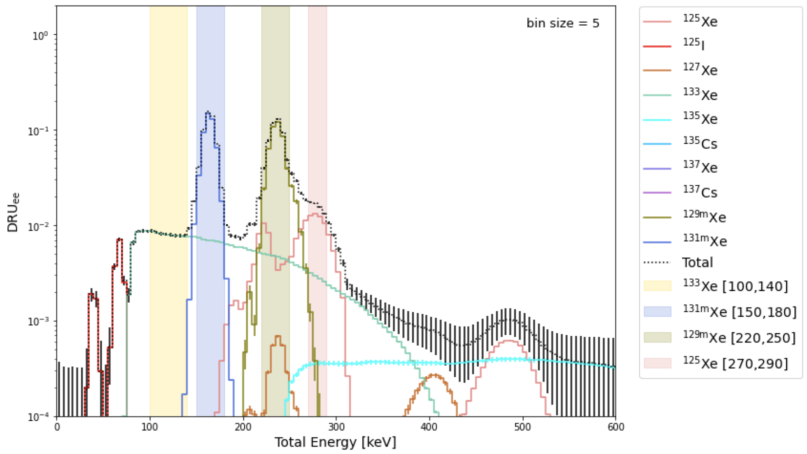

Figure 3-6: Identical to Fig. 3-3, but with counting regions for ^{131m}Xe, ^{129m}Xe, and ^{125}Xe highlighted where each respective decay dominates the spectrum.

counted. In the region between 100 and 300 keV$_{ee}$ for the simulated decay spectra, decay signatures for four different isotopes dominate different energy regions in the spectrum. Each of these regions is highlighted in Figure 3-6. In these "counting" regions (with the exception of ^{133}Xe, the dominant isotope is responsible for most, but not all, of the decay counts. The ^{133}Xe counting region has only negligible contributions from non-^{133}Xe isotopes. In order to separate the total number of decays in each energy region and discern how many belong to each isotope, the simulated BACCARAT decay spectra were utilized to establish the fraction of each decay spectrum in each counting region. The ^{125}Xe counting region in the [270, 290] keV$_{ee}$ range has non-negligible contributions from ^{125}Xe and ^{133}Xe decay only. By subtracting out the ^{133}Xe contribution, the total number of ^{125}Xe decays can therefore be calculated and its contributions to the other counting bins subsequently excluded.

Table 3.4 lists the fraction of individual decay spectra in each counting region. These fractions applied to the combined energy spectrum for the October WS period output the

Decay Contribution Breakdown in Counting Regions

Energy Region	Fraction of ^{133}Xe Decay	Fraction of ^{125}Xe Decay	Fraction of ^{129m}Xe Decay	Fraction of ^{131m}Xe Decay
[100,140]	0.228	$< 10^{-6}$	$< 10^{-6}$	$< 10^{-6}$
[270,290]	0.041	0.297	$< 10^{-6}$	$< 10^{-6}$
[220,250]	0.100	0.214	0.869	$< 10^{-6}$
[150,180]	0.148	0.003	$< 10^{-6}$	0.970

Table 3.4: ^{133}Xe overlaps will all other decay counting regions, and the ^{125}Xe spectrum also overlaps with the ^{129m}Xe counting region. These ratios stem from a simulated calibration and subsequent 2-week decay period using 1×10^7 neutrons simulated down the LUX neutron conduit, then subsequently scaled to match the data.

total decays counted for each nuclei during the two-week period following calibration. Looking at Table 3.5, one can see that the number of ^{125}Xe nuclei produced by inelastic neutron scattering expected to decay during the WS period is zero within a margin of error. This matches expectations, as stable ^{125}Xe nuclei should only be produced by radiative capture.

Oct. WS Decays from Atoms Produced by Neutron Capture or Inelastic Scattering

Isotope	Total Counted Decays (10^3)	Expected Decays from Neutron Capture (10^3)	Decays from Inelastic Scattering (10^3)
^{125}Xe	0.570 ± 0.320	0.460 ± 0.058	0.110 ± 0.325
^{129m}Xe	2.10 ± 0.10	0.161 ± 0.020	1.94 ± 0.11
^{131m}Xe	2.68 ± .08	0.279 ± 0.035	2.40 ± 0.09

Table 3.5: Calculation of decays from atomic states produced by inelastic neutron scatters.

With the decays from nuclei produced by inelastic neutron scattering isolated for ^{129m}Xe and ^{131m}Xe, equations 3.5 and 3.6 can once again be cycled through. The inelastic neutron scattering production rates can then be combined with the fast neutron flux through the detector to calculate the inelastic neutron scattering production cross sections of ^{129m}Xe and ^{131m}Xe, as given in Table 3.6.

^{129m}Xe and ^{131m}Xe Production: Inelastic Neutron Scattering Cross Sections

Isotope	Nuclei Produced by DD (10^3)	Production Rate ($cm^{-3}s^{-1}$) (10^{-7})	Parent Fractional Abundance	Neutron Cross Section (mb)
^{129m}Xe	3.45 ± 0.20	1.39 ± 0.08	0.264	1.47 ± 0.08
^{131m}Xe	5.21 ± 0.19	1.88 ± 0.07	0.212	2.52 ± 0.09

Table 3.6: Calculation of production rate and neutron cross section presuming a 13 day calibration period and a 10.6 decay period, with a 2.45 MeV neutron flux of 2.56 ± 1.00 $\times 10^{-2}$ neutrons/cm^2/s

3.5 Results and Discussion

In the previous section, inelastic neutron scattering production cross-sections for ^{129m}Xe and ^{131m}Xe were calculated to be 1.47 ± 0.07 mb and 2.52 ± 0.08 mb, respectively. These values were calculated using data from the LUX detector, and although simulations were used to better understand the composition of the real data spectrum, the simulated spectra were independently scaled and spread using energy-dependent Gaussian convolutions to match the data as closely as possible. In effect, the independent scaling of each spectra shielded the analysis from any errors stemming from the GEANT4-provided production rates.

Figure 3-7 plots the October WS combined energy spectrum against the total simulated decay spectrum. Rather than scaling each individual isotope spectra to fit the data spectrum's features, the entire simulated spectrum has been scaled by a flat factor, fitting the simulation to the data in regions dominated by ^{133}Xe and ^{125}Xe. The cross-sections used by GEANT4 to simulate the production of ^{133}Xe and ^{125}Xe are assumed to be accurate. With this uniform scaling, the simulated prediction for the ^{129m}Xe decay peak dramatically exceeds the real peak from the LUX data. The ^{131m}Xe simulated decay peak also exceeds its real

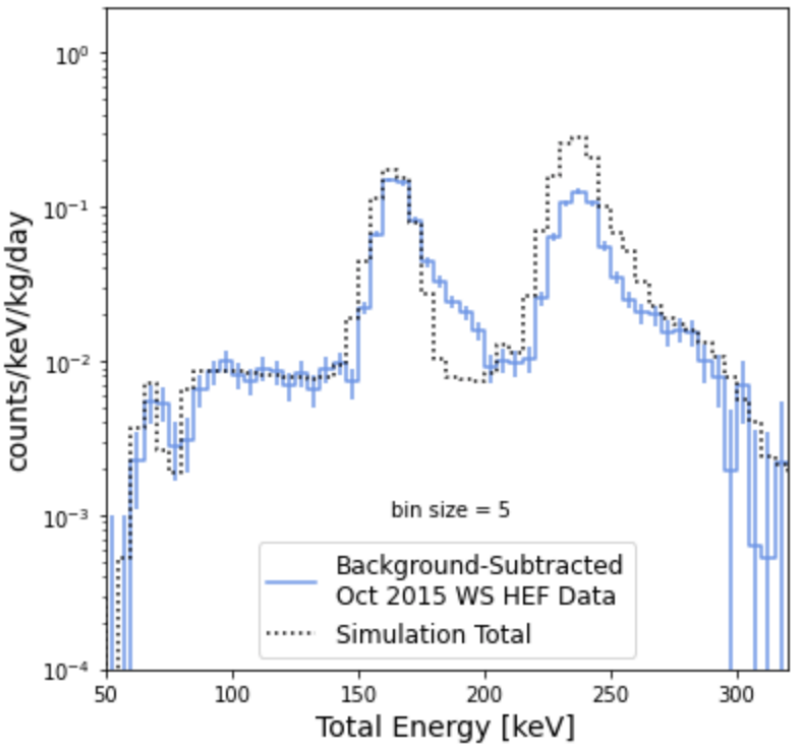

Figure 3-7: The total simulated spectra scaled by a flat factor, matching the neutron intensity of the simulation to the real calibration flux, fits the data, except in the ^{129m}Xe and ^{131m}Xe peaks.

counterpart, indicating that GEANT4 may be providing incorrect values for the inelastic neutron scattering production cross sections of both isotopes.

In order to determine the cross-section used for both metastable isotopes in GEANT4, the process described above for the real data is repeated for the simulated data. The results are reported in Table 3.7. For both ^{131m}Xe and ^{129m}Xe, the inelastic neutron scattering production cross sections used in the simulation exceed those calculated from the data. These results suggest that GEANT4's inelastic final state calculations for ^{129m}Xe and ^{131m}Xe are not accurate.

Comparison to GEANT4 Cross-Section

Isotope	Neutron Cross Section from Data (mb)	Neutron Cross Section From GEANT4 (mb)
^{129m}Xe	1.47 ± 0.08	6.56 ± 0.07
^{131m}Xe	2.52 ± 0.09	4.39 ± 0.07

Table 3.7: Calculation of the simulation cross-section utilized the real 2.45 MeV neutron flux of 2.56 ± 1.00 $\times 10^{-2}$ neutrons/cm^2/s and scaled simulated counts by a factor of 0.45.

3.6 Conclusions and Further Work

This analysis reports the first measurement of the inelastic neutron scattering production cross sections of ^{131m}Xe and ^{129m}Xe. These cross-sections were calculated using data from the LUX detector's 2014-2016 data collection run. The cross-sectional values calculated from the LUX data disagree with the effective cross-sections used by GEANT4 to simulate xenon activation and the resulting decay spectrum. These results are significant, and indicate that caution should be exercised when using GEANT4 to study metastable xenon production in detectors. In order to shore up these results, further research should be done to better account for background sources in the real data. In particular, the decay shoulder to the right of the ^{131m}Xe peak indicates a gap in this analysis' understanding of decays occurring in the energy region of interest.

Bibliography

[1] Ade, P. A. R., Aghanim, N., Armitage-Caplan, C., Arnaud, M., Ashdown, M., Atrio-Barandela, F., Aumont, J., Baccigalupi, C., Banday, A. J. and et al. [2014], 'Planck2013 results. xvi. cosmological parameters', *Astronomy Astrophysics* **571**, A16.

URL: *http://dx.doi.org/10.1051/0004-6361/201321591*

[2] Agency, U. S. E. P. [2016], 'A Citizen's Guide To Radon: The Guide To Protecting Yourself And Your Family From Radon'.

[3] Akerib, D., Alsum, S., Araújo, H., Bai, X., Balajthy, J., Baxter, A., Bernard, E., Bernstein, A., Biesiadzinski, T., Boulton, E. and et al. [2020], 'Discrimination of electronic recoils from nuclear recoils in two-phase xenon time projection chambers', *Physical Review D* **102**(11).

URL: *http://dx.doi.org/10.1103/PhysRevD.102.112002*

[4] Akerib, D., Araújo, H., Bai, X., Bailey, A., Balajthy, J., Bedikian, S., Bernard, E., Bernstein, A., Bolozdynya, A., Bradley, A. and et al. [2014], 'First results from the lux dark matter experiment at the sanford underground research facility', *Physical Review Letters* **112**(9).

URL: *http://dx.doi.org/10.1103/PhysRevLett.112.091303*

[5] Akerib, D., Araújo, H., Bai, X., Bailey, A., Balajthy, J., Bernard, E., Bernstein, A., Bradley, A., Byram, D., Cahn, S. and et al. [2015], 'Radiogenic and muon-induced

backgrounds in the lux dark matter detector', *Astroparticle Physics* **62**, 33–46.

URL: *http://dx.doi.org/10.1016/j.astropartphys.2014.07.009*

[6] Akerib, D., Bai, X., Bedikian, S., Bernard, E., Bernstein, A., Bolozdynya, A., Bradley, A., Byram, D., Cahn, S., Camp, C. and et al. [2013], 'The large underground xenon (lux) experiment', *Nuclear Instruments and Methods in Physics Research Section A: Accelerators, Spectrometers, Detectors and Associated Equipment* **704**, 111–126.

URL: *http://dx.doi.org/10.1016/j.nima.2012.11.135*

[7] Akerib, D., Bai, X., Bernard, E., Bernstein, A., Bradley, A., Byram, D., Cahn, S., Carmona-Benitez, M., Carr, D., Chapman, J. and et al. [2013], 'An ultra-low background pmt for liquid xenon detectors', *Nuclear Instruments and Methods in Physics Research Section A: Accelerators, Spectrometers, Detectors and Associated Equipment* **703**, 1–6.

URL: *http://dx.doi.org/10.1016/j.nima.2012.11.020*

[8] Akerib, D. S., Bai, X., Bedikian, S., Bernard, E., Bernstein, A., Bradley, A., Cahn, S. B., Carmona-Benitez, M. C., Carr, D., Chapman, J. J., Chan, Y.-D., Clark, K., Classen, T., Coffey, T., Dazeley, S., deViveiros, L., Dragowsky, M., Druszkiewicz, E., Faham, C. H., Fiorucci, S., Gaitskell, R. J., Gibson, K. R., Hall, C., Hanhardt, M., Holbrook, B., Ihm, M., Jacobsen, R. G., Kastens, L., Kazkaz, K., Lander, R., Larsen, N., Lee, C., Leonard, D., Lesko, K., Lyashenko, A., Malling, D. C., Mannino, R., McKinsey, D., Mei, D., Mock, J., Morii, M., Nelson, H., Nikkel, J. A., Pangilinan, M., Parker, P. D., Phelps, P., Shutt, T., Skulski, W., Sorensen, P., Spaans, J., Stiegler, T., Svoboda, R., Smith, A., Sweany, M., Szydagis, M., Thomson, J., Tripathi, M.,

Verbus, J. R., Walsh, N., Webb, R., White, J. T., Wlasenko, M., Wolfs, F. L. H., Woods, M., Uvarov, S. and Zhang, C. [2012], 'Radio-assay of titanium samples for the lux experiment'.

[9] Akerib, D. S. et al. [2015], 'Radiogenic and Muon-Induced Backgrounds in the LUX Dark Matter Detector', *Astropart. Phys.* **62**, 33–46.

[10] Aprile, E., Aalbers, J., Agostini, F., Alfonsi, M., Althueser, L., Amaro, F., Antochi, V., Angelino, E., Angevaare, J., Arneodo, F. and et al. [2020], 'Excess electronic recoil events in xenon1t', *Physical Review D* **102**(7).
URL: *http://dx.doi.org/10.1103/PhysRevD.102.072004*

[11] Bertone, G. and Hooper, D. [2018], 'History of dark matter', *Reviews of Modern Physics* **90**(4).
URL: *http://dx.doi.org/10.1103/RevModPhys.90.045002*

[12] Bradley, A. W. [2014], LUX Thermosyphon Cryogenics and Radon-Related Backgrounds for the First WIMP Result, PhD thesis, Case Western Reserve U.

[13] Collaboration, G. [n.d.], *GEANT4: Physics Reference Manual*, GEANT4.

[14] Freese, K. [2017], 'Status of dark matter in the universe', *International Journal of Modern Physics D* **26**(06), 1730012.
URL: *http://dx.doi.org/10.1142/S0218271817300129*

[15] Hu, W. [2008], 'Lecture notes on cmb theory: From nucleosynthesis to recombination'.

[16] Huang, D. [2020], Ultra-Low Energy Calibration of the LUX and LZ Dark Matter Detectors, PhD thesis, Brown U.

[17] Knoll, G. F. [2000], *Radiation Detection and Measurement*, third edn, John Wiley Sons, Inc., New York.

[18] Kudryavtsev, V. A. [2019], 'Recent Results from LUX and Prospects for Dark Matter Searches with LZ', *Universe* **5**(3), 73.

[19] Malling, D. C. [2014], Measurement and Analysis of WIMP Detection Backgrounds, and Characteri- zation and Performance of the Large Underground Xenon Dark Matter Search Experiment, PhD thesis, Brown U.

[20] *Nuclear Physics and Reactor Theory 1.1: Neutron Cross-Sections, Neutron Density and Neutron Flux (Module 3)* [1996], Complete Published Course Modules.

[21] Rubin, V. C., Ford, Jr., W. K. and Thonnard, N. [1978], 'Extended rotation curves of high-luminosity spiral galaxies. IV. Systematic dynamical properties, Sa through Sc', *Astrophys. J. Lett.* **225**, L107–L111.

[22] Zwicky, F. [1937], 'On the Masses of Nebulae and of Clusters of Nebulae', **86**, 217.